

Applications of Elemental Bio-Imaging and Development of Novel Quantification Methods

by

Christine Austin

A thesis submitted for the

Degree of Doctor of Philosophy (Science)

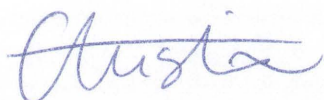
University of Technology, Sydney

2011

Certificate of authorship and originality

I certify that the work in this thesis has not previously been submitted for a degree nor has it been submitted as part of the requirements for a degree except as fully acknowledged within the text.

I also certify that the thesis has been written by me. Any help that I have received in my research work and the preparation of the thesis itself has been acknowledged. In addition, I certify that all the information sources and literature used are indicated in the thesis.



Christine Austin

29/07/2011

DATE

A little learning is a dang'rous thing;

Drink deep, or taste not the Pierian Spring:

There shallow draughts intoxicate the brain,

And drinking largely sobers us again.

-Alexander Pope, *An Essay on Criticism* (1711)

Acknowledgements

As with any project of this magnitude, a number of people need to be acknowledged for their contributions. This thesis would not have been possible without the support of my supervisors Philip Doble and Andrew McDonagh. Thank you for your guidance and encouragement throughout this project.

I owe a great deal of gratitude to Fred Fryer for his generously and expediently given advice, comments and aid in instrument trouble shooting, experimental design and interpretation of results. Ric Wuher was also an enormous help in developing the XRM technique and fostering excitement for the project.

Laboratory work would not have run so smoothly without Jim Keegan and Ilona Kramer who maintained the labs and instruments with utmost professionalism. I am also grateful to Alison Beavis, Dominic Hare, David Bishop and Jessica Lear for their involvement in many ICP-MS discussions and lab aid. Thanks also to Tristan Rawling for fruitful collaborations and Brian Reedy for help with macros and imaging software.

I would like to thank Bill Robinson and Andrew Rozelle of Stanford University and Ross Crawford from QUT for the provision of samples for this research. I also appreciate the staff at the Department of Forensic Medicine for allowing us to use their facilities to prepare our samples.

Thank you to all the post-graduate students who were a great source of support and escape from daily frustrations. Special thanks go to the residence of 4.30 and in particular Jess, Julia, Lisa and Tristan – your distractions were certainly beneficial to my mental health. Ellen was especially helpful in keeping me on track in my final months with a combination of positive motivation (McFlurries) and strictly enforced deadlines.

To my family, I can't thank you enough for all the love and support you've given me during my candidature. Mum and dad have not only supported me emotionally (and nutritionally) but also financially which enabled me to focus my time on this research as well as have the means to travel as the opportunities arose. You guys rock!

Table of contents

CERTIFICATE OF AUTHORSHIP AND ORIGINALITY	II
ACKNOWLEDGEMENTS	IV
TABLE OF CONTENTS	V
LIST OF FIGURES	IX
LIST OF TABLES	XVIII
LIST OF PUBLICATIONS AND CONFERENCE PRESENTATIONS	XXI
ABBREVIATIONS	XXII
ABSTRACT	XXV
CHAPTER 1: ELEMENTAL IMAGING OF BIOLOGICAL MATERIAL.....	2
1.1 THE ELEMENTS AND HUMAN HEALTH	2
1.1.1 <i>Calcium Crystals and Osteoarthritis</i>	5
1.2 ELEMENTAL BIO-IMAGING TECHNIQUES	9
1.2.1 <i>Staining Methods</i>	11
1.2.2 <i>Electron Microprobe</i>	11
1.2.3 <i>Proton Beam Microprobe</i>	12
1.2.4 <i>Synchrotron-based X-ray fluorescence</i>	13
1.2.5 <i>Secondary Ion Mass Spectrometry</i>	14
1.2.6 <i>Laser Ablation-Inductively Coupled Plasma-Mass Spectrometry</i>	15
1.3 INDUCTIVELY COUPLED PLASMA—MASS SPECTROMETRY	16
1.3.1 <i>Sample Introduction</i>	17
1.3.2 <i>Ion Formation</i>	19
1.3.3 <i>Plasma-MS interface</i>	21
1.3.4 <i>Mass Analyser</i>	23
1.4 LASER ABLATION	26
1.4.1 <i>The Ablation Process</i>	30

1.4.2	<i>Lasers</i>	33
1.4.3	<i>Cell Design and Transport Volume</i>	36
1.4.4	<i>Carrier Gas</i>	40
1.5	ELEMENTAL BIO-IMAGING BY LA-ICP-MS	44
1.5.1	<i>Polyacrylamide Gel Electrophoresis</i>	46
1.5.2	<i>Elemental Labelling</i>	48
1.5.3	<i>Xenobiotic Metal Distribution</i>	50
1.5.4	<i>Soft Tissue Imaging</i>	50
1.5.5	<i>Hard Tissue Imaging</i>	53
1.6	PROJECT AIMS	58
CHAPTER 2: CRYSTAL IMAGING IN BIOLOGICAL MATERIAL		60
2.1	INTRODUCTION	60
2.1.1	<i>Synovial Fluid Composition</i>	61
2.1.2	<i>Methods for Crystal Detection</i>	62
2.1.3	<i>X-ray Mapping</i>	73
2.1.4	<i>LA-ICP-MS</i>	75
2.1.5	<i>Aims and Objectives</i>	88
2.2	EXPERIMENTAL.....	89
2.2.1	<i>Synovial Fluid Samples and Preparation</i>	89
2.2.2	<i>Bio-Imaging of Synovial Fluid by LA-ICP-MS</i>	90
2.2.3	<i>X-Ray Mapping of Dried Droplets</i>	91
2.2.4	<i>LA-ICP-MS Conditions for Interference Assessment</i>	92
2.2.5	<i>LA-ICP-MS Imaging Conditions</i>	93
2.2.6	<i>Data Processing</i>	94
2.3	RESULTS AND DISCUSSION	96
2.3.1	<i>Crystal Imaging by XRM</i>	96
2.3.2	<i>ICP-MS Interference Removal</i>	105

2.3.3	Crystal Imaging by LA-ICP-MS	115
2.3.4	Synovial Fluid Imaging.....	117
2.4	CONCLUSIONS.....	123
CHAPTER 3: QUANTIFICATION WITH SPIKED POLYMER FILMS.....		126
3.1	INTRODUCTION	126
3.1.1	LA-ICP-MS Quantification Procedures	127
3.1.2	Thin Polymer Film Production by Spin Coating	139
3.1.3	Polymers for Spin Coating	144
3.1.4	Aims and Objectives	145
3.2	EXPERIMENTAL.....	147
3.2.1	Film Optimisation	147
3.2.2	Film Characterisation	149
3.2.3	Film Quantification	149
3.2.4	Quantification of Tissue Standards.....	150
3.3	RESULTS AND DISCUSSION	153
3.3.1	PMMA Thin Film Standards	153
3.3.2	Water Soluble Polymer Films.....	157
3.3.3	Quantification of Tissue Standards.....	163
3.4	CONCLUSIONS.....	167
CHAPTER 4: FACTORS AFFECTING QUANTIFICATION WITH AN INTERNAL STANDARD		169
4.1	INTRODUCTION	169
4.1.1	Factors Affecting Internal Standardisation.....	170
4.1.2	¹³ C as an IS for Elemental Bio-Imaging.....	172
4.1.3	Internal Standards in Underlying Thin Films.....	174
4.2	EXPERIMENTAL.....	177
4.2.1	Instrumental	177
4.2.2	Factors Affecting Internal Standardisation.....	177

4.2.3	<i>Internal Standards in Underlying Thin Films</i>	180
4.3	RESULTS AND DISCUSSION	184
4.3.1	<i>Factors Affecting Internal Standardisation</i>	184
4.3.2	<i>Internal Standard Approaches with Thin Films</i>	202
4.4	CONCLUSIONS.....	213
CHAPTER 5: CRYSTAL IMAGING IN CARTILAGE WITH QUANTIFICATION		216
5.1	INTRODUCTION	216
5.1.1	<i>Depth Analysis</i>	216
5.1.2	<i>Aims and Objectives</i>	217
5.2	EXPERIMENTAL.....	218
5.2.1	<i>Tissue Preparation</i>	218
5.2.2	<i>Alizarin Red S Staining</i>	218
5.2.3	<i>LA-ICP-MS Imaging Conditions</i>	218
5.2.4	<i>Standards</i>	219
5.3	RESULTS AND DISCUSSION	221
5.3.1	<i>Crystal Imaging</i>	221
5.3.2	<i>Depth Profiles</i>	225
5.4	CONCLUSIONS.....	228
CHAPTER 6: CONCLUSIONS AND RECOMMENDATIONS		230
6.1	CONCLUSIONS.....	230
6.2	RECOMMENDATIONS.....	232
REFERENCES.....		236

List of figures

Figure 1: A healthy knee joint (a) and joint damage caused by osteoarthritis (b) and rheumatoid arthritis(c). In osteoarthritis the cartilage breaks down and the bone becomes rough. Rheumatoid arthritis is characterised by inflammation of the joint lining. Adapted from Summit Medical Group [23].....	6
Figure 2: Schematic of an ICP-MS (Agilent Technologies 7500) showing the four main compartments; sample introduction system, torch (where ions are formed), plasma-MS interface and mass analyser. From Agilent Technologies (2007) [75].....	17
Figure 3: Typical nebuliser (a) and spray chamber (b) for liquid sample introduction to ICP-MS. The schematic represents a pneumatic nebuliser and double-pass spray chamber, the most commonly used system for liquid sample introduction.	18
Figure 4: Schematic of the ICP torch. Adapted from New Mexico State University (2006) [78]	19
Figure 5: Plasma-MS interface in an Agilent 7500 series ICP-MS. From Agilent Technologies (2007) [75].....	22
Figure 6: Schematic of quadrupole mass filter. From School of Chemistry (2009) [82]	24
Figure 7: Diagram of a typical laser ablation system. Adapted from Günther et al. (1999) [83]	26
Figure 8: Growth of LA-ICP-MS publications from 1985 – 2009 (a) and pie chart of LA-ICP-MS applications between 1985 and October 2010 (b). Source: ISI Web of Knowledge, key words 'LA-ICP-MS', 'laser ablation ICP-MS' and 'laser ablation inductively coupled plasma mass spectrometry' used in (a) and with subject areas geological (), biological (), environmental (), forensic () and materials ()used in (b).....	27
Figure 9: Transport efficiency of fs-laser ablation in He and Ar cell gases. From Garcia et al. (2009) [89].....	29

Figure 10: Theoretical generation of ablation plume showing expansion (a) and ablation plume from fs ablation of steel (b) and plastic (c) showing shock wave, vapour generation and particle ejection. Adapted from Photonics Online [105] and Paul Scherrer Institut [106]	31
Figure 11: Laser – material interactions with (a) nanosecond and (b) femtosecond pulse duration lasers. From Fernandez et al. (2007) [109]	35
Figure 12: Signal variation at different sampling positions in a circular ablation cell. Adapted from Bleiner and Günther (2001) [117]	37
Figure 13: Volume-optional and low memory cell incorporating open and closed cell designs. From Liu et al. (2007) [119].....	38
Figure 14: Visible light images of ablation craters formed in (a) Ar and (b) He atmospheres. The thickness of the condensation deposits is indicated by the interference fringes. From Eggins et al. (1998) [135]	41
Figure 15: Typical workflow of elemental bio-imaging by LA-ICP-MS; sample preparation of soft tissue section, analysis by LA-ICP-MS, collection of element time resolved profiles and importation into imaging software to generate an element map.....	44
Figure 16: 2D gel separation of proteins (a) and the LA-ICP-MS analysis of selected protein spots (b). Adapted from Becker and Jakubowski (2009) [60]	47
Figure 17: Photomicrograph (left) of Ni-labelled mouse brain section and corresponding ^{60}Ni image (right). Scale on right represents high (red) to low (purple) signal intensity. Adapted from Hutchinson et al. (2005) [169]	49
Figure 18: Illustration of labelling and the analysis of a microarray of labelled protein spots. Adapted from Hu et al. (2007) [170].....	49
Figure 19: Photographs of sentinel lymph node partially replaced by metastatic melanoma observed in the upper two thirds of the image (a, b) and element distributions determined by LA-ICP-MS showing a decrease in C and P signal intensities (c-f). From Hare et al. (2009) [179]	52
Figure 20: Quantitative ($\mu\text{g g}^{-1}$) element maps in a tobacco leaf (Mg is given as intensity in counts per second). Adapted from Becker et al. (2010) [185]	53

Figure 21: Diagram of a knee joint showing the synovial cavity. Adapted from Bjorklund (2010) [199].....	61
Figure 22: Monosodium urate (a) and CPPD (b) crystals under CPLM. The comparatively weaker birefringence and higher morphological variation of the CPPD crystals can be clearly seen. Some CPPD crystals show no birefringence. Modified from Yavorskyy et al. (2008) [32]	63
Figure 23: Clumps of BCP crystals stained red with alizarin red S. Modified from Punzi et al. (2005) [21].....	65
Figure 24: IR spectra from different calcium phosphates. Adapted from Dieppe and Calvert (1983) [29].....	66
Figure 25: Raman reference spectra of synthetic BCP, HA, CPPD and MSU crystals. Adapted from Yavorskyy et al. (2008) [32].....	67
Figure 26: TEM (a) and SEM (b) images of CPPD crystals. Adapted from Dieppe et al. (1979) [220]	68
Figure 27: AFM images of HA (a) and CPPD (b) crystals in SF. Adapted from Blair et al. (1995) [221]	70
Figure 28: Radiograph of the lateral compartment of the knee joint showing the typically linear calcification indicative of CPPD deposits. Adapted from Dieppe and Calvert (1983) [29]	71
Figure 29: Resolution of polyatomic interference and analyte ion based on KED. Modified from Hill (2007) [76].....	82
Figure 30: Thermochemical properties of some analyte (solid circles) and polyatomic interference (open circles) ions. First ionisation potentials are represented in (a). The horizontal lines represent the FIP of the reaction gas. Ions above a horizontal line are thermodynamically favourable for charge transfer with the indicated neutral. (b) Oxygen-atom affinities are represented in (b). The horizontal lines indicate the O-atom affinities of gases having one less oxygen than the indicated neutral. Ions above a line are	

thermodynamically favourable to extract an oxygen atom from the indicated neutral. Adapted from Tanner et al. (2002) [241].....	85
Figure 31: X-ray maps of Na, Cl, P and Ca in SF doped with CPP (horizontal width of field 210 μm).....	96
Figure 32: X-ray spectra of sample taken over CPP particle area (blue) and particle-free area (black).....	97
Figure 33: QXRM of Cl, Na, P, K, Ca and S in SF doped with CPP. The grey scale represents 0 – 100 wt % for each element.	98
Figure 34: QXRM of Cl, Na, P, K, Ca and S in SF doped with CPP. The grey scale has been adjusted for each element to improve image contrast.	98
Figure 35: Pseudo coloured map of Ca, P and Cl in SF with a close up of particles (right). Yellow regions (due to the mixture of green (P) and red (Ca) represent CaP crystals (horizontal width of field 210 μm)	99
Figure 36: SEM image of (a) CPP and (b) CPMM powder showing size of particles. Microbar equivalent to 50 μm in both images.	99
Figure 37: Pseudo colour maps of Ca, P and Cl in SF samples doped with CPP (a) and CPMM (b) (horizontal width of field 820 μm). CPP and CPMM particles appear yellow in both images.	100
Figure 38: 2D scatter diagrams of Ca, P, Na and Cl in SF doped with CPP.....	100
Figure 39: Pixels selected from scatter diagrams superimposed on electron image of SF doped with CPP (horizontal width of field 210 μm).....	101
Figure 40: QXRM of Cl, Na, P, K, Ca and S in natural SF1. The grey scale has been adjusted for each element to improve image contrast.....	102
Figure 41: Surface electron image (a) and pseudo colour map (b) of CaP particles in SF1 (horizontal width of field 90 μm)	102

Figure 42: Pseudo colour map of CaP particles in the high Cl matrix of natural SF samples (horizontal width of field 900 μm (a) and 90 μm (b))	103
Figure 43: X-ray spectra for SF2 collected from a particle (blue) and surrounding area (black)	103
Figure 44: SEM image of salt crystals formed in the centre of natural SF (a) and pseudo colour map of natural SF showing salt phases (b). The different salt phases can be seen from the mixing of colours assigned to each element; sodium chloride appears yellow due to the mixing of green (Na) and red (Cl) while potassium chloride appears purple due to the mixing of blue (K) and red. (Bar represents 100 μm in (a), horizontal width of field 900 μm in (b)).	104
Figure 45: 2D scatter images of Ca, P and Cl in a natural SF sample	105
Figure 46: Signal-to-background ratio of (a) ^{40}Ca () and ^{56}Fe () in NIST 612 and (b) ^{44}Ca (), ^{56}Fe (), ^{52}Cr (X) and ^{88}Sr () in thin PMMA film standard	106
Figure 47: Elemental distribution maps of ^{43}Ca , ^{31}P , ^{24}Mg , ^{88}Sr and ^{66}Zn in a cartilage section from a patient diagnosed with OA.....	116
Figure 48: Elemental distribution maps of ^{43}Ca , ^{31}P , ^{24}Mg , ^{88}Sr and ^{63}Cu obtained by LA-ICP-MS analysis of a dried droplet of SF from a patient diagnosed with OA	118
Figure 49: Elemental distribution maps of ^{43}Ca , ^{31}P , ^{24}Mg and ^{88}Sr in a drop of synthetic synovial fluid without sample pre-treatment (top row), and with filtration (bottom row) ...	119
Figure 50: Overlay of LA-ICP-MS and LM image showing region of interest (ROI) selection for statistical analysis of spiked SF samples	120
Figure 51: Comparison of expected versus calculated concentrations for Mg in two predominantly CaCO_3 CRMs determined using external calibration with glass CRMs (diamonds), pressed CaCO_3 powdered standards (squares) and other CaCO_3 matrix predominant CRMs (triangles). From Craig et al. (2000) [286]	129
Figure 52: Experimental set-up of laser ablation chamber with nebuliser for IS aerosol introduction. Adapted from Pickhardt et al. (2006) [304].....	132

Figure 53: Schematic of the major process involved in spin coating. From Norrman (2005) [353]	140
Figure 54: Schematic representation of striation development during spin coating. Adapted from Birnie (2001) [360]	143
Figure 55: Thickness of 5 ($\times 10^{-1}$), 10 () and 15 % (w/w) () PMMA films($n = 3$) as a function of spin speed.....	154
Figure 56: Effect of xylene content on analyte concentration () and film thickness (\times) ($n = 3$)	154
Figure 57: Surface roughness (a) and film edge formations (b) determined by AFM	155
Figure 58: The effect of spin solution analyte concentration on CF determined from dye UV-Vis absorption ($n = 3$)	157
Figure 59: Workflow of quantification of analytes in soft tissue by calibration with thin film standards. From Austin et al., (2010) [388]	164
Figure 60: Diagram of SAM formation on gold coated substrate	175
Figure 61: Connection between ablation cell outlet and ICP-MS used to monitor the effect of temperature on ^{13}C signal drift.	178
Figure 62: Ruthenium phthalocyanine complexes used for molecular thin films	182
Figure 63: Average ^{13}C signal intensity at different temperatures for Tygon® (), steel () and PTFE (X) ($n = 7$)	185
Figure 64: $^{13}\text{C}/^{14}\text{C}$ (a) and $^{13}\text{C}/^{12}\text{C}$ (b) signal ratio as a function of tissue thickness at different mass peak width settings of W-10 % 0.80 amu (), 0.65 amu () and 0.40 amu (X) ($n = 6$). ..	189
Figure 65: Plot of ^{13}C (), ^{59}Co () and ^{63}Cu (X) signal intensity from thin film as a function of ablation line width in (a) a standard ablation and (b) large format cell ($n = 3$).	190
Figure 66: Normalised ^{63}Cu and ^{66}Zn signal intensity ratios as a function of ablation line width using the standard ablation cell (a, b) and LFC (c, d). Analytes in the thin film were normalised	

to ^{13}C (), ^{59}Co (), ^{85}Rb (X) and ^{197}Au (). In all graphs the $^{63}\text{Cu}/^{13}\text{C}$ and $^{66}\text{Zn}/^{13}\text{C}$ ratios are $\times 10^{-1}$ (n = 3).	191
Figure 67: Normalised ^{56}Fe (a) and ^{63}Cu (b) signal intensity ratios in tissue (10 μm thick) as a function of ablation line width in the LFC. Analytes are normalised to ^{13}C (), ^{59}Co () and ^{85}Rb (X) (n = 3).	192
Figure 68: Analyte responses to changes in plasma forward power using thin film standards. Raw data without normalisation ^{13}C (), ^{59}Co (), ^{85}Rb (X) and ^{197}Au () (a), ^{85}Rb normalised to ^{13}C () and ^{59}Co () (b), ^{197}Au normalised to ^{13}C () and ^{59}Co () (c) and ^{63}Cu normalised to ^{13}C () and ^{59}Co () (d) (n = 3).	193
Figure 69: Line scan RSDs at each plasma power setting produced from ablation of thin film for (a) ^{63}Cu and (b) ^{197}Au with no IS () and normalised to ^{13}C (), ^{52}Cr (), ^{53}Cr (), ^{59}Co () and ^{89}Y () ISs (n = 3).	194
Figure 70: Analyte response from thin film at different omega lens setting: a) signal intensities of ^{13}C ($\times 10^{-1}$) (), ^{24}Mg (), ^{59}Co (), ^{85}Rb (X) and ^{197}Au (), b) ^{24}Mg with normalisation, c) ^{85}Rb with normalisation and d) ^{63}Cu with normalisation to ^{13}C ($\times 10$) (), ^{59}Co () and ^{89}Y (X) (n = 3).	196
Figure 71: Line scan RSDs at each omega lens setting produced from ablation of thin film: ^{197}Au (a) and ^{63}Cu (b) with no IS () and normalised to ^{13}C (), ^{52}Cr (), ^{53}Cr (), ^{59}Co () and ^{89}Y () ISs (n = 3).	197
Figure 72: $^{63}\text{Cu}/^{13}\text{C}$ response from signal intensity, element FIP and ablation volume, and mass bias experiments at different mass resolutions: W-10 % 0.80 amu (), 0.65 amu () and 0.40 amu (X) (n = 6).	197
Figure 73: Ablation cell sampling locations for (a) standard cell and (b) large format cell	198
Figure 74: Signal instability from ablation of a thin film across sampling locations in a standard ablation cell: a) elements used as ISs (^{13}C (), ^{53}Cr () and ^{89}Y (X)), b) ^{63}Cu with normalisation, c) ^{101}Ru with normalisation and d) ^{57}Fe with normalization to ^{13}C (), ^{53}Cr () and ^{89}Y (X) (n = 3).	199

Figure 75: Comparison of raw () and IS normalised signal stability of analytes in standard ablation cell from ablation of a thin film. Analytes are normalised to ^{13}C (), ^{52}Cr (), ^{53}Cr (), ^{89}Y () and ^{101}Ru () ISs (n = 3).	199
Figure 76: Comparison of raw and IS normalised signal stability of analytes in LFC cell from ablation of a thin film. Analytes are normalised to ^{13}C (), ^{52}Cr (), ^{53}Cr (), ^{89}Y () and ^{101}Ru () ISs (n = 3).	200
Figure 77: Surface coverage of thin films of gold at 3 nm (a), 5 nm (b) and 10 nm (c) thickness. Scale bar on all images is 500 nm (horizontal width of field 1.49 μm)	203
Figure 78: Surface density of SAM film over time for complex 2	205
Figure 79: Example of a non-uniform film that was not washed after immersion in SAM solution. Aggregation of the complex can be seen from the increase in the ^{101}Ru signal intensity	205
Figure 80: Line scan uniformity of ^{13}C (blue), ^{59}Co (purple), ^{63}Cu (red), ^{89}Y (green) and ^{197}Au (orange) across pre-ablated channel (a) and ^{63}Cu signal (red) after normalisation to ^{13}C (blue), ^{59}Co (purple), ^{89}Y (green) and ^{197}Au (orange) (b).	209
Figure 81: IS and analyte signal intensity as a function of the distance transverse by the laser. The edge of the tissue is ablated at approximately 2.7 mm across the PMMA ISF (a) and 2.3 mm across the PAA ISF (b).	212
Figure 82: Histological stain and depiction of the zones in hyaline cartilage. Compositional and orientation changes are illustrated by macromolecule and collagen content (left), and fibre (middle) and cell (right) content and orientation. Adapted from Athanasiou (2010) [205] ..	217
Figure 83: Work flow of final analysis of cartilage samples. Step 1 involved the preparation of thin film standards by spin coating; Step 2 represents the preparation of samples with the removal of cartilage from the bone, sectioning and finally staining with Alizarin Red S; Step 3 represents the analysis of samples and standards by LA-ICP-MS and Step 4 shows the conversion of line scan data into images with a scale added after calibration plots were constructed from the thin film standards.	220
Figure 84: ARS stained cartilage section	221

Figure 85: Quantified elemental maps and ARS LM image of cartilage section. Laser parameters: 25 μm spot size, 25 $\mu\text{m s}^{-1}$ scan speed.....	222
Figure 86: Elemental maps and ARS LM image of cartilage section. Laser parameters: 40 μm spot size, 40 $\mu\text{m s}^{-1}$ scan speed.....	223
Figure 87: Localised regions of high Ca unrelated in CaP deposits. Laser parameters: 25 μm spot size, 25 $\mu\text{m s}^{-1}$ scan speed.....	224
Figure 88: ^{44}Ca map overlaid on ARS LM image and RGB composite images showing element correlation. Laser parameters: 25 μm spot size, 25 $\mu\text{m s}^{-1}$ scan speed.....	225
Figure 89: Light microscope image of cartilage section cut perpendicular to bone.....	225
Figure 90: High resolution image of element distribution in cartilage with depth. Pixel size is approximately 25 \times 23 μm . Laser parameters: 25 μm spot size, 25 $\mu\text{m s}^{-1}$ scan speed.....	226
Figure 91: Depth distribution maps of articular cartilage, acquired with a laser spot size of 40 μm and scan speed of 40 $\mu\text{m s}^{-1}$. Cartilage is orientated with bone (B) on the left and synovial cavity (S) on the right. A light microscopy image of the section was also included (bottom right). Laser parameters: 40 μm spot size, 40 $\mu\text{m s}^{-1}$ scan speed.....	227

List of tables

Table 1: Elements found in the human body and their functions or medicinal applications.....	4
Table 2: Selected characteristics of arthritis associated calcium crystals [28, 29, 31, 32]	7
Table 3: Figures of merit for techniques used for elemental imaging of soft tissues [5, 41, 42, 56, 57]	14
Table 4: Summary of the laser parameters that affect fractionation, approaches used to minimise the effect and an explanation of the phenomenon. Adapted from Sylvester (2008) [142]	43
Table 5: Summary of LA-ICP-MS bio-imaging applications	55
Table 6: Advantages and disadvantages of techniques used for crystal detection and identification	72
Table 7: Common polyatomic and isobaric interferences on analyte isotopes	77
Table 8: Detection of Ca by ICP-MS with figures of merit	86
Table 9: Interferences on major Ca and Sr isotopes [261, 266]	87
Table 10: LA-ICP-MS parameters for elemental bio-imaging of spiked and natural SF	90
Table 11: LA-ICP-MS parameters used for investigation of the cool plasma technique for interference attenuation	92
Table 12: LA-ICP-MS parameters used for optimisation of reaction/collision cell parameters	93
Table 13: Typical LA-ICP-MS parameters used for elemental bio-imaging of cartilage samples	94
Table 14: Signal-to-background ratio for selected elements at various collision/reaction gas flows	109
Table 15: Isotope ratio % difference from literature value [274]	111

Table 16: Comparison of standard, cool plasma and CRC techniques for the analysis of Ca .	112
Table 17: Normalised Ca and Sr intensities and isotope ratios over increasing analyte Ca/Sr or Sr/Ca ratio	113
Table 18: Statistical p value derived from student's t-test or Mann-Whitney test of crystal type for specific resolutions and ROI type	121
Table 19: Statistical p value derived from student's t-test or Mann-Whitney test of ROI type for specific resolutions and crystal type	122
Table 20: Summary of quantification methods for LA-ICP-MS reported in the literature	137
Table 21: Polymers suitable for spin coating and relevant properties	146
Table 22: LA-ICP-MS parameters used for the analysis of thin polymer films and quantification of tissue standards with PMMA film standards.....	151
Table 23: Summary of important characteristics of films prepared from different water soluble polymers	158
Table 24: Effect of heat treatment on the thickness, uniformity and dryness of PEI films	159
Table 25: Solvent properties used to select co-solvent for improved film uniformity	161
Table 26: Film thickness and surface roughness from 5 % PAA solutions in 1:1 water : co-solvent.....	161
Table 27: Cu and Zn concentrations determined from LA-ICP-MS and SN-ICP-MS techniques ($\mu\text{g g}^{-1}$)	165
Table 28: p-values from the comparison of means by t-tests of LA-ICP-MS and SN-ICP-MS concentrations	166
Table 29: Standard operating parameters for LA-ICP-MS of thin polymer films and soft tissue	177
Table 30: LA-ICP-MS conditions for analysis of molecular thin films.....	182

Table 31: % RSDs of elements determined at different temperatures using a calibration curve constructed at RT with different ISs	186
Table 32: Concentration of analytes determined at different temperatures with Tygon®, PTFE and steel tubing	187
Table 34: Abundance sensitivity determined at different mass peak width at 10 % peak height values	188
Table 35: Analyte signal intensity ratios from NIST 612 CRM recorded at different intervals and % RSD of ratios over the intervals during an elemental bio-imaging experiment.....	195
Table 36: (a) Precision (% RSD) and (b) accuracy (% difference between quantified and actual concentration) of quantification of analytes with different ISs.....	201
Table 37: Line scan precision and signal intensity of Au.....	203
Table 38: Surface density and normalised Ru signal intensity of different Pc-Ru complexes used to form molecular thin films on gold	206
Table 39: Line scan precision (% RSD) of raw and normalised analyte signal intensities from a tissue standard placed on top of a PMMA ISF.....	209
Table 40: Precision of analyte determinations in a tissue standard placed atop PMMA ISFs	210
Table 41: Difference in determined and known concentration in a tissue standard	211
Table 42: Typical LA-ICP-MS parameters used for elemental bio-imaging of cartilage samples	219
Table 43: Element concentrations in PMMA standards	219

List of Publications and Conference Presentations

1. Austin C., D. Hare, A.L. Rozelle, W.H. Robinson, R. Grimm and P. Doble, *Metallomics*, Elemental bio-imaging of calcium phosphate based crystal deposits in knee samples from arthritic patients, 2009, **1**, (2), 142-147 (Results published in this paper are included in Chapter 2).
2. Rawling T., C.E Austin, D. Hare, P.A. Doble, H.M. Zareie, and A.M. McDonagh, *Nano Research*, Thin Films of Ruthenium Phthalocyanine Complexes, 2009, **2**, (9), 678-687 (Results published in this paper are included in Chapter 4).
3. Austin C., D. Hare, T. Rawling, A.M. McDonagh and P. Doble, *Journal of Analytical Atomic Spectrometry*, Quantification method for elemental bio-imaging by LA-ICP-MS using metal spiked PMMA films, 2010, **25**, (5), 722-725 (Results published in this paper are included in Chapter 3).
4. Austin C., F. Fryer, J. Lear, D. Bishop, D. Hare, T. Rawling, L. Kirkup, A. McDonagh and P. Doble, *Journal of Analytical Atomic Spectrometry*, Factors affecting internal standard selection for quantitative elemental bio-imaging of soft tissues by LA-ICP-MS, 2011, **26**, (7), 1494-1501 (Results submitted in this paper are included in Chapter 4).
5. Austin C., Hare D., Rozelle A.L., Robinson W.H., Grimm R. and Doble P., *International Symposium on Metallomics 2009*, Cincinnati, USA, Elemental bio-imaging of calcium phosphate based crystal deposits in knee samples from arthritic patients. Oral presentation.
6. Austin C., Rawling T., Hare D., McDonagh A., Doble P., *International Symposium on Metallomics 2009*, Cincinnati, USA, Quantification method for elemental bio-imaging by LA ICP-MS using spiked thin films. Oral presentation.

Abbreviations

AFM	Atomic force microscopy
ARS	Alizarin red S
BCP	Basic calcium phosphate
CaP	Calcium phosphate-based
CF	Concentration factor
CPPD	Calcium pyrophosphate dihydrate
CPLM	Compensated polarised light microscopy
CPM	Chemical phase mapping
CPMM	Calcium phosphate monobasic monohydrate
CPP	Calcium pyrophosphate
cps	Counts per second
CRC	Collision/reaction cell
CRM	Certified reference material
csv	Comma separated value
DRC	Dynamic reaction cell
DMF	N,N-Dimethylformamide
DMSO	Dimethyl sulfoxide
EHDP	^{14}C -ethane-1-hydroxy-1,1-disphonate
EDS	Energy dispersive spectrometer
EDTA	Ethylenediaminetetraacetic acid
EMPA	Electron microprobe analysis
ESEM	Environmental scanning electron microscope
ETV	Electrothermal vaporisation
FAA	Flame atomic absorption
FI	Flow injection
FIP	First ionisation potential
FSXRM	Full spectrum X-ray mapping
FTIRM	Fourier transform infrared microscopy
HA	Hydroxyapatite
HPLC	High pressure liquid chromatography
ICP-MS	Inductively coupled plasma-mass spectrometry
i.d.	Internal diameter

IDMS	Isotope dilution mass spectrometry
IS	Internal standard
ISF	Internal standard film
KED	Kinetic energy discrimination
LA	Laser ablation
LFC	Large format cell
LOD	Limit of detection
LOQ	Limit of quantification
MALDI	Matrix assisted laser desorption/ionisation
MRI	Magnetic resonance imaging
MSU	Monosodium urate
m/z	Mass-to-charge ratio
Nd:YAG	Neodymium doped yttrium aluminium garnet
NIST	National Institute of Standards and technology
OA	Osteoarthritis
PA	Pulse/analogue
PAA	Poly(acrylic acid)
PAGE	Polyacrylamide gel electrophoresis
P/B	Peak-to-background ratio
PEI	Poly(ethyleneimine)
PEO	poly(ethylene oxide)
PhCl	Chlorobenzene
PIXE	Particle induced X-ray emission
PLM	Polarised light microscopy
PMMA	Poly(methylmethacrylate)
PsA	Psoriatic arthritis
PVA	Poly(vinyl alcohol)
qMS	Quadrupole mass spectrometer
QUT	Queensland University of Technology
QXRM	Quantitative X-ray mapping
RA	Rheumatoid arthritis
RBS	Rutherford backscattering spectrometry
REE	Rare earth element
RGB	Red, green, blue

ROI	Region of interest
RSD	Relative standard deviation
RSF	Relative sensitivity factor
RT	Room temperature
RuPc	Ruthenium phthalocyanine
SAM	Self assembled monolayer
S/B	Signal-to-background ratio
SEM	Scanning electron microscopy
SFMS	Sector field mass spectrometry
SIMS	Secondary ion mass spectrometry
SN	Solution nebulisation
STEM	Scanning transmission electron microscopy
SXRF	Synchrotron-based X-ray fluorescence
TDS	Total dissolved solids
TEM	Transmission electron microscopy
TOF	Time of flight
W-10 %	Peak width at 10 % of the peak height
WDS	Wave dispersive spectrometer
XAS	X-ray absorption spectroscopy
XRD	X-ray diffraction
XRM	X-ray mapping
ZAF	Atomic number, absorption and fluorescence

Abstract

This thesis investigates an elemental bio-imaging technique that may be used to detect calcium phosphate-based (CaP) crystals in cartilage. CaP crystals are associated with osteoarthritis and define a subset of other arthritides. It is not yet known if these crystals play a direct role in disease conception/progression or are markers of joint damage. Improving our understanding of the processes involved in crystal formation and their relationship to arthritis may lead to the identification of therapy targets or biomarkers, enabling the development of effective treatments or early detection and monitoring of the disease. This is hindered by the small size and complex biological matrix which make crystal detection difficult using traditional technologies. Greater understanding may be achieved through the application of novel technologies, such as those described in this thesis, to crystal detection in biological materials.

Metallomics is an emerging field first defined in the early 2000's. It is the study of free metals and metal containing species; their interactions, transformations and functions in biological systems. The study of metals is of great importance since many metals play essential roles in maintaining physiological functions or cause toxicity in organisms. Spatially resolved elemental maps offer unique insights into the role of metals at the tissue and cellular level. The production of element distribution maps is termed elemental bio-imaging.

Laser ablation-inductively coupled plasma-mass spectrometry (LA-ICP-MS) is an elemental bio-imaging technique capable of providing elemental maps, increasingly applied to the study of metals and non-metals in biological samples. LA-ICP-MS offers the benefits of direct multi-element analysis of solid samples with minimal sample preparation, high sensitivity and detection of trace, minor and major elements. In this study LA-ICP-MS was applied to the detection and identification of calcium phosphate-based (CaP) crystals in human cartilage and synovial fluid samples.

The LA-ICP-MS elemental bio-imaging method was developed to detect and identify CaP crystals in cartilage and synovial fluid. The analysis of Ca is hindered by interfering species in the mass spectrum (e.g. $^{40}\text{Ar}^+$, $^{12}\text{C}^{16}\text{O}_2^+$). Two methods of interference reduction were investigated to improve Ca detection: cool plasma and collision/reaction cell (CRC). The CRC method gave the best improvements in signal-to-background ratios, detection limits and

isotope ratio accuracy. The affect of Ca ($^{44}\text{Ca}_2^+$) and Sr-based ($^{88}\text{Sr}^{2+}$) interferences on Sr and Ca isotope signal intensities was also investigated. Both elements produced a negligible effect on the respective analyte signal intensities.

Development of a new quantification procedure was undertaken to further improve the LA-ICP-MS imaging method by defining a scale for easy crystal detection. Current quantification procedures are time consuming and laborious. Thin polymer films spiked with analytes and prepared by the spin coating technique were validated using tissue standards and finally used to quantify cartilage sections stained for CaP crystals. The films were prepared from a solution containing 10 % PMMA, 40 % xylene and 50 % chlorobenzene. The new quantification procedure also enabled the inclusion of multiple internal standards (IS) by placing the tissue sample on top of the film. Factors affecting the efficacy of ISs were also investigated. A close match in mass was the dominating factor in selecting optimal analyte/IS pairings and ablation cell design was also identified as an important factor in IS selection. For soft tissue analysis, ^{13}C was found to be an effective IS but an element closer in mass to the analyte provided better signal compensation.

The developed LA-ICP-MS elemental bio-imaging technique was successfully applied to the detection of CaP crystals in cartilage. This is the first study to show the correlation between CaP crystals and Sr and therefore this technique may provide new insights into the processes involved in crystal generation and their relationship to arthritis.